

# **Barometric pressure variations associated with eastern Pacific tropical instability waves**

Meghan F. Cronin

*NOAA Pacific Marine Environmental Laboratory, Seattle, Washington*

Shang-Ping Xie

*International Pacific Research Center and Department of Meteorology, University of Hawaii,  
Honolulu, Hawaii*

Hiroshi Hashizume

*Jet Propulsion Laboratory, California Institute of Technology, Pasadena, California*

*J. Climate, In Press*

Submitted: September 26, 2002

Revised: March 10, 2003

Accepted: March 24, 2003

*Corresponding author address:* Dr. Meghan F. Cronin, NOAA Pacific Marine Environmental  
Laboratory; 7600 Sand Point Way NE; Seattle, WA 98115, USA. E-mail:  
[cronin@pmel.noaa.gov](mailto:cronin@pmel.noaa.gov).

**Abstract.** Barometric pressure, surface temperature and wind time series in the eastern equatorial Pacific are analyzed to determine if oceanic tropical instability wave (TIW) sea surface temperature variations cause barometric pressure gradients large enough to influence the atmospheric boundary layer. During the study period from April 2001 through September 2002, 11 TIWs propagated westward past 110°W, causing a spectral peak at 20-30 days in the sea surface temperature (SST) meridional difference between 2°N, 110°W and 0°, 110°W. Likewise, the meridional pressure difference also had a spectral peak in the 20-30 day TIW band. Cross-spectral analysis shows that within the TIW band, SST-induced pressure variations were roughly  $-0.1 \text{ hPa } ^\circ\text{C}^{-1}$  in magnitude. The resulting pressure gradient force is comparable in magnitude to other terms in the meridional momentum balance. Implications about the role of the boundary-layer capping in the adjustment to SST forcing are discussed.

## 1. Introduction

As the cold tongue of water extends westward along the equator, westward propagating, crest-like wave patterns form on the sea surface temperature (SST) front (Fig. 1). Tropical instability waves (TIWs) are hydrodynamic instabilities caused by the increased horizontal and vertical shears (Philander 1978; Qiao and Weisberg 1995; Masina et al. 1999). Although of oceanic origin, TIW variability can project onto the atmosphere, causing cloud (Deser et al. 1993; Hashizume et al. 2001), heat flux (Thum et al. 2002), and wind variations (Hayes et al. 1989; Xie et al. 1998; Liu et al. 2000; Wentz et al. 2000; Chelton et al. 2001; Hashizume et al. 2002) with similar 20-30 day periodicities. In this analysis we investigate mechanisms by which SST influences the atmospheric boundary layer (ABL). In particular, we use moored barometric pressure data to evaluate SST-induced pressure gradients.

According to the Lindzen and Nigam (1987) boundary layer model (hereinafter referred to as LN), low-level winds are forced by pressure gradients set by the SST field. The LN model assumes that the ABL is well mixed, and that air-sea temperature difference is spatially and temporally uniform. Further, to obtain realistic winds, the model assumes that the boundary layer height adjusts rapidly (~30 minutes) to SST anomalies.

Although convenient, these assumptions are not necessarily realistic. As noted by Battisti et al. (1999), for quasi-steady solutions, a more realistic adjustment time is ~1-2 days, and certainly not less than the timescale associated with the life cycle of deep convective mixing, i.e., 8-12 hours (Bretherton et al. 1995). Likewise, sounding data show that stratification and thus static stability within the ABL is strongly influenced by SST (Bond 1992; Anderson 2001; Yin and Albrecht 2000; Hashizume et al. 2002). Over warm water, air-sea temperature difference is large and negative and the ABL is neutrally stratified. Over cool water south of the equator and

in the equatorial cold tongue, air-sea temperature difference is small, and the ABL is often weakly stably stratified.

Using COADS data, Wallace et al. (1989; hereinafter referred to as WMD) showed that SST influences on surface boundary layer static stability and vertical mixing had an order-one effect on low-level wind anomalies. Over cold water, increased stratification decouples the upper portion of the ABL from the lower portion, resulting in weak winds near the surface. Over warm water, turbulent mixing brings strong southeasterly winds down to the surface. As illustrated in Fig. 2, satellite wind and SST fields regressed to TIW-band SST variations at  $2^{\circ}\text{N}$ ,  $110^{\circ}\text{W}$  show southeasterly wind anomalies in phase with positive SST anomalies, consistent with the WMD mechanism. In contrast, LN would predict wind anomalies maximized over SST gradients.

On and south of the equatorial front, the ABL is almost always capped by a strong temperature inversion. Because surface pressure is a measure of the column-integrated mass, boundary layer height variations will also contribute to surface pressure gradients. Indeed, a zonal section of soundings, transecting several TIWs in September 1999 (Hashizume et al. 2002), showed shallow ABL over the cold crests and deep ABL over the warm troughs of TIWs. Although severely contaminated by the semidiurnal tide, there was no detectable TIW signal in the surface pressure. Had the pressure gradient from the boundary height variations completely opposed the TIW thermal pressure gradients? Do TIWs have a surface pressure signal?

Over the ocean, surface pressure is sparsely sampled and tends to be dominated by atmospheric weather disturbances such as the easterly waves. However, since April 2001, barometric pressure sensors have been deployed at  $110^{\circ}\text{W}$  buoys at the equator and  $2^{\circ}\text{N}$ , making it possible for the first time to detect the TIW signal in surface pressure. This paper presents an

analysis of these new measurements and studies the TIW effect on surface pressure. We show that a TIW surface pressure signal exists and may even be a first-order term in the surface momentum budget.

## **2. Data**

As part of the Eastern Pacific Investigation of Climate Processes (EPIC) process study (Raymond et al. 2002; Cronin et al. 2002), beginning in April 2001, Tropical Atmosphere and Ocean (TAO) moorings at  $2^{\circ}\text{N}$ ,  $110^{\circ}\text{W}$  and  $0^{\circ}$ ,  $110^{\circ}\text{W}$  were equipped with high quality pressure sensors. Standard surface measurements on TAO moorings include wind speed and direction, relative humidity, air temperature ( $T_a$ ), and 1-m SST (McPhaden et al. 1998). As with standard TAO measurements, daily averaged barometric pressure measurements were telemetered to shore via Service Argos. The study period for this analysis is therefore from April 2001 through September 2002.

Following Hashizume et al. (2001), QuikSCAT satellite winds and Tropical Rain Measuring Mission (TRMM) Microwave Imager (TMI) SST are used to determine the surface wind field coherent with TIW SST variability for the 2001 TIW season from June through December. Both fields are mapped onto a  $0.5^{\circ} \times 0.5^{\circ} \times 3$  day grid. After removing a  $12^{\circ}$ -longitude moving average and smoothing with a 3-point moving average filter, the band-passed fields are then regressed against a band-passed TMI SST time series at  $2^{\circ}\text{N}$ ,  $110^{\circ}\text{W}$ . The standard deviation of the  $2^{\circ}\text{N}$ ,  $110^{\circ}\text{W}$  reference time series is 0.9K. The resulting regression coefficients for the SST and wind fields are shown in Fig. 2. For more details on this procedure see Hashizume et al. (2001). These wind fields will be used in Section 3c to determine the

relative importance of the SST-induced pressure gradient in the TIW momentum budget.

Daily averaged barometric pressure ( $P_0$ ) at  $2^\circ\text{N}$ ,  $110^\circ\text{W}$  and  $0^\circ$ ,  $110^\circ\text{W}$  (Fig. 3) have substantial variability from large-scale upper atmosphere waves that influence both sites coherently. However, there also appear to be variations between these two sites associated with changes in the SST ( $T_s$ ) frontal structure. In the following discussion,  $\Delta$  denotes the  $2^\circ\text{N}$  minus equatorial value and is proportional to the finite difference estimate of the meridional gradient. Step-like changes in pressure difference  $\Delta P_0$  can be attributed to sensor resolution. Paroscientific Inc. pressure sensors have resolution of 0.1 hPa and 0.01% accuracy. Clearly, if sensors with less accuracy and precision had been used, the pressure gradient signal would not have been detected.

Consistent with warmer temperatures to the north, surface pressure is nearly always lower at  $2^\circ\text{N}$  than at the equator. While TIWs are most easily seen in the  $2^\circ\text{N}$  SST time series (Fig. 3b), TIW variability can also be seen in the pressure difference time series (Fig. 3c). . As a TIW crest passes  $110^\circ\text{W}$ ,  $2^\circ\text{N}$  (e.g. in mid-December 2001 for the TIW shown in Fig. 1),  $T_s$  cools, and  $\Delta T_s$  and  $\Delta P_0$  approach zero. As a TIW trough passes  $110^\circ\text{W}$ ,  $2^\circ\text{N}$ ,  $T_s$  and  $\Delta T_s$  increase, and  $\Delta P_0$  becomes large and negative (lower pressure at  $2^\circ\text{N}$  relative to equator). During the 17-month record, roughly 11 TIWs crossed  $110^\circ\text{W}$ . During the warm season between January and April 2002, when there was little difference between SST at  $2^\circ\text{N}$  and the equator, no TIWs formed and the pressure difference between the two sites was minimal (Fig. 3).

Although  $T_a$  tracks  $T_s$ , there are differences between  $\Delta T_a$  and  $\Delta T_s$  (Fig. 3d) associated with variations in air-sea temperature difference. Consistent with reduced stability over warm SST, air-sea temperature difference is largest over the warm water and smallest over cool water. On average,  $T_a - T_s$  is  $-1^\circ\text{C}$  at  $2^\circ\text{N}$ ,  $110^\circ\text{W}$ , but only  $-0.3^\circ\text{C}$  at the equator,  $110^\circ\text{W}$ . As the SST

front crosses  $2^\circ\text{N}$ ,  $T_a - T_s$  varies, giving rise to a TIW signal in the air-sea temperature difference (Thum et al. 2002).

### 3. Results

#### *a. Spectral analyses*

Spectral and coherence analyses are used to isolate the TIW signal in the pressure and temperature time series. Power spectra were computed on demeaned daily averaged time series using the Welch method. In particular, each 128-day fft includes 64-day overlap and is tapered with a 128-day Hanning window. As shown in Fig. 4,  $\Delta T_a$ ,  $\Delta T_s$  and  $\Delta P_0$  all have spectral peaks in the TIW band (21-32 day periodicities). TIW variance is computed by integrating the power spectra over the TIW frequency band. Overall variance and TIW variance for  $\Delta T_a$  is smaller than for  $\Delta T_s$ . Within the TIW band,  $\Delta T_s$  variance is  $0.3^\circ\text{C}^2 \sim (0.6^\circ\text{C})^2$ ,  $\Delta T_a$  variance is  $0.1^\circ\text{C}^2 \sim (0.3^\circ\text{C})^2$ , and  $\Delta P_0$  variance is  $0.01 \text{ hPa}^2 \sim (0.10 \text{ hPa})^2$ .

To estimate the SST-induced pressure gradient within the TIW band, the transfer function between temperature and pressure differences (i.e.,  $\Delta T_s$  and  $-\Delta P_0$ ) is computed by dividing their cross-spectral density by the power spectral density of  $\Delta T_s$ . This is equivalent to the square root of the coherence multiplied by the ratio of the power spectral density for  $\Delta P_0$  to the power spectral density for  $\Delta T_s$ . Within the TIW band,  $\Delta T_s$  and  $-\Delta P_0$  are highly coherent (Fig. 5) and the transfer function between  $\Delta T_s$  and  $-\Delta P_0$  is  $0.11 \text{ hPa/K}$ . Curiously,  $-\Delta P_0$  leads  $\Delta T_s$  by up to four days, which raises questions about causality. However, the paradox is resolved by noting that hydrostatic pressure depends upon the virtual potential temperature of the air, rather than the temperature of the sea surface. Surface air temperature slightly leads SST, an effect of advection

by the mean easterlies (Small et al. 2003).

With SST replaced by air temperature, the coherence with  $-\Delta P_0$  is increased and the transfer function between  $\Delta T_a$  and  $-\Delta P_0$  increased to 0.24 hPa/K, which is closer to the value predicted by LN (see the next section for a comparison with LN). Likewise on TIW timescales,  $\Delta T_a$  and  $-\Delta P_0$  are more in phase, as expected. The improvement is an indication that air-sea temperature difference was not constant, and is a reflection on the variability of the atmospheric stability. The phase shift between air temperature and sea temperature could be due in part to advective processes (Thum et al. 2002). Southeasterly prevailing winds could cause a westward phase shift in the air temperature TIW pattern which then causes the  $-\Delta P_0$  to lead  $\Delta T_s$ .

*b. Thermal pressure gradient versus interfacial pressure gradient*

To gain insight into the mechanisms by which SST influences the pressure gradient, it is useful to consider the expected temperature-induced hydrostatic pressure gradient of a weakly stratified atmospheric boundary layer that is capped by an inversion of mean height  $H$ . Integrating the hydrostatic relation with respect to height from the top of the boundary layer at  $z = H + h$ , down to the surface, and assuming that the pressure gradient above the inversion vanishes and  $h \ll H$  (much as in the shallow-water, reduced-gravity formulation), then the  $z = 0$  surface pressure gradient can be expressed as:

$$\nabla P_0 = \rho_0 g H \frac{\nabla \theta_{v0}}{\theta_{v0}} + \rho_0 g^* \nabla h , \quad (1)$$

where  $\nabla$  is the gradient operator,  $\rho_0$  and  $\theta_{v0}$  are the typical density and virtual potential temperature in the ABL,  $g$  is gravity,  $g^* = g d\bar{\theta}_v / \theta_{v0}$  is the reduced gravity (with  $d\bar{\theta}_v$  the jump



across the inversion). The first term on the right-hand-side of (1) will be referred to as the “thermal pressure gradient” and the second term in (1) will be referred to as the “interfacial pressure gradient”.

To compare the thermal pressure gradient to the temperature-induced pressure variations computed in the previous section 3a, we divide (1) by  $\nabla\theta_v$ . Note that  $\nabla\theta_v$  is approximately equivalent to  $\nabla T_a$ . Assuming  $H \sim 1$  km,  $\theta_{v0} = 296$ K (and corresponding  $\rho_0 = 1.20$  kg m<sup>-3</sup>), the scale value for the thermal pressure gradient ( $\rho_0 g H / \theta_{v0}$ ) is 0.4 hPa/K, almost four times larger than the observed transfer function between  $\theta T_s$  and  $-\theta P$  (0.11 hPa/K) but less than a factor of two greater than the observed transfer function between  $\theta T_a$  and  $-\theta P$  (0.24 hPa/K).

Assuming  $g^* = 0.2$  ms<sup>-2</sup> for  $d\bar{\theta}_v = 6$  K and  $\theta_{v0} = 296$ K, the interfacial pressure term could compensate for the thermal pressure term (resulting in no surface pressure gradient) if a 1 K SST gradient was associated with a height adjustment of 165 m (i.e., ~15% of the ABL height). Interestingly, the effect of this would be a shift in the dynamical influence of SST on pressure from within the atmospheric mixed layer to near the inversion layer. The relatively large value of the observed meridional surface pressure gradient suggests that the meridional height variations are either much smaller than this scale of height adjustment, or have different phasing than the thermal pressure effect (see Section 4).

### *c. Importance to momentum balance*

To appreciate the size of the SST-induced meridional pressure gradient and determine if it is large enough to influence ABL winds, we compare the TIW meridional pressure gradient to

other terms in the momentum balance. The vertically integrated TIW meridional momentum balance near the equator can be written as:

$$(\mathbf{u} \cdot \nabla v)' = -\frac{1}{r} \frac{\partial P'}{\partial y} + \frac{t_h'}{rH_m} - \frac{t_0'}{rH_m}, \quad (2)$$

where  $\mathbf{u}$ ,  $v$  and  $P$  are the layer-averaged vector wind, meridional wind and pressure; and  $t_0$  and  $t_h$  are the meridional wind stress at the air-sea interface and at the top of the mixed layer at  $z = H_m$ .

Primes indicate TIW variability. It is assumed that within a degree or two of the equator the Coriolis acceleration can be neglected.

Our goal is not to close the momentum balance, but rather to compare the magnitude of the observed TIW pressure gradient to the amplitude of other terms in the budget. For this purpose, we use the TIW-regressed wind field shown in Fig. 2 and the June through December 2001 mean wind fields shown in Fig. 6. The TIW advection term along  $1^\circ\text{N}$  computed from these fields has an amplitude of  $15 \times 10^{-6} \text{ m s}^{-2} \text{ K}^{-1}$ .

For a mixed layer that is a fraction of the height of the ABL, the mixed layer-averaged pressure gradient in (2) will be approximately the value of the surface pressure gradient  $\partial P' / \partial y \sim \partial P_0' / \partial y$ . We assume here that pressure at the top of the ABL varies on planetary scales, i.e., on scales much larger than in the boundary layer frontal region. Thus, from Fig. 5 and with  $\Delta y = 2.22 \times 10^5 \text{ m}$ , the SST-induced pressure gradient forcing can be computed as  $41 \times 10^{-6} \text{ m s}^{-2} \text{ K}^{-1}$ , which is more than twice as large as the advective terms shown in Fig. 6.

The TIW-meridional stress at the air-sea interface  $t_0'$  can be estimated very crudely in terms of a mean drag coefficient  $C_d$  ( $\sim 1.3 \times 10^{-3}$ ), as:

$$t_0' = r C_d \sqrt{u^2 + v^2} v'. \quad (3)$$

Thus, assuming a mean wind speed of  $6 \text{ m s}^{-1}$ , the TIW SST-induced surface stress (drag) forcing in (2) has a magnitude of roughly  $6.2 \times 10^{-6} \text{ m s}^{-2} \text{ K}^{-1}$  for a mixed layer of mean height  $H_m \sim 500 \text{ m}$ . Thus, according to this simple scale analysis, the SST-induced pressure gradient forcing is more than six times larger than the SST-induced surface drag.

The amplitude of mixing from aloft (term involving  $t_h'$  in (2)) is difficult to estimate. Based upon WMD arguments, if this term dominates, then southeasterly wind anomalies will be in phase with  $T_s$  anomalies. This phasing is in qualitative agreement with the observed phasing shown in Fig. 2. However, closer inspection of Fig. 2 shows that maximum meridional wind anomalies are slightly south of the maximum temperature anomaly, consistent with the effects of the pressure gradient forcing. The thermal pressure gradient tends to enhance the mixing-induced acceleration of the southerly winds south of the maximum positive temperature anomaly but reduces it to the north. Thus, it is likely that the pressure gradient force is an order one process in the atmospheric boundary layer's adjustment to tropical instability wave SST variations.

#### 4. Discussion

Wind and SST data from the  $2^\circ\text{N}$ ,  $110^\circ\text{W}$  and  $0^\circ$ ,  $110^\circ\text{W}$  moorings were used in some of the earliest studies of TIWs (Halpern 1987, Hayes et al. 1989). Because no pressure data were available until recently, previous analyses have had to rely upon subtle phase distinctions to evaluate the relative role of thermal-pressure gradients (e.g., LN) versus stability-dependent mixing from aloft (e.g., WMD). As discussed above, the meridional wind variations due to these two processes can be difficult to distinguish based on phasing relative to SST anomalies, particularly near the equator. Furthermore, slight shifts in the air-temperature phasing relative to

SST due to advection or other processes (Thum et al. 2002) can make these phase analyses difficult to interpret.

Beginning in April 2001, pressure sensors were added to the  $0^{\circ}$ ,  $110^{\circ}\text{W}$  and  $2^{\circ}\text{N}$ ,  $110^{\circ}\text{W}$  TAO moorings in support of EPIC. These new data show that while locally, barometric pressure variability is dominated by large-scale variability induced by dynamical processes above the boundary layer (e.g., Raymond et al. 1998) the TIW signal is detectable and dominates the meridional pressure gradients on SST frontal scales ( $\sim 200$  km). Scale analysis of the meridional momentum budget shows that the resulting pressure gradient is an order one process in the atmospheric mixed layer's adjustment to TIW SST forcing. Results from a recent model simulation support our scale analysis. Using a high-resolution regional atmospheric model, Small et al. (2003) show that the westward shift of air temperature and hence thermal pressure relative to SST anomalies produces an anomalous wind pattern that is roughly in phase with SST, a phase relation that has traditionally been attributed to vertical mixing and wind shear adjustment but in fact is consistent with the pressure-driving mechanism for wind variability.

Between  $0^{\circ}$ ,  $110^{\circ}\text{W}$ , and  $2^{\circ}\text{N}$ ,  $110^{\circ}\text{W}$ , the SST-induced *meridional* pressure gradient is slightly less than predicted by LN, but more than expected based on the Hashizume et al. (2002) sounding data. Hashizume et al. (2002) showed that the “interfacial-pressure gradient” tended to cancel the “thermal pressure gradient” so that the *zonal* pressure gradient at the surface was weak and incoherent with the TIW pattern. The apparent disagreement between our results and the Hashizume et al. (2002) study can be reconciled by considering the different adjustment processes in the zonal and meridional directions.

While air temperature in the ABL and hence the thermal pressure are strongly tied to the

local SST, we speculate that the meridional adjustment of the inversion height occurs on scales much larger than the ocean frontal scale ( $\sim 200$  km), say at the atmospheric radius of deformation<sup>1</sup> ( $\sim 800$  km for  $g^*$  and  $H$  values listed above). As a result, the equator– $2^\circ\text{N}$  difference in the inversion height is small and the barometric pressure gradient in the meridional direction is dominated by the thermal pressure gradient. In the zonal direction, by contrast, the TIW wavelength is comparable to the inversion adjustment scale and hence, the thermal and interfacial pressure gradients may compensate each other as suggested by Hashizume et al. (2002). As discussed in 3b, the sea level pressure gradient results not only from ABL temperature changes but reflects the dynamic adjustment of the capping inversion. Our hypothesis regarding the inversion adjustment and the resultant surface pressure effect needs to be tested in numerical models. We note, however, that many full-physics models have difficulty simulating the strong inversion and hence may overestimate the thermal pressure gradient effect.

Tropical ocean and atmosphere are strongly coupled in general and it is very difficult to isolate cause and effect. However, because TIWs are generated by ocean dynamics to the first order, by analyzing atmospheric variability coherent with SST variability in this frequency band we can isolate the effects of the ocean on the atmosphere. While the TIW variance in the surface wind is very small (10-15% of the mean speed), there is large TIW variance in the wind

---

<sup>1</sup> There are other possible length scales, such as that for damped gravity waves of phase speed  $c$ :  $c/\varepsilon$ , with  $\varepsilon$  being the boundary-layer damping rate. Chelton et al. (2001) estimate that the adjustment time of Betts (1983) is about 14 hours, which gives a horizontal adjustment scale of 706 km for the reduced gravity and boundary-layer height given above. The horizontal scale becomes 252 km if one uses a typical surface wind speed of  $5 \text{ m s}^{-1}$  instead of gravity wave speed.

divergence and curl patterns, which can drive variations in clouds (Deser et al. 1993; Hashizume et al. 2001) and ocean currents (Chelton et al. 2001, Kessler et al. 2002).

*Acknowledgments.* The pressure sensors were purchased through a NSF grant to C. Bretherton. Processing and maintenance of the pressure sensors have been provided by the TAO project office at NOAA PMEL. The TMI data are obtained via ftp from the Remote Sensing System website. Helpful comments were provided by S. Esbensen and an anonymous reviewer. SPX was supported by NASA through its QuikSCAT mission and grant NAG5-10045, NOAA PACS Program (NA17RJ1230) and by Frontier Research System for Global Change. HH's contribution was performed at JPL, California Institute of Technology under contract with NASA. This is PMEL contribution #2499, IPRC contribution #xxx and SOEST contribution #yyy.

## References

- Anderson, S. P., 2001: On the atmospheric boundary layer over the equatorial front. *J. Climate*, **14**, 1688-1695.
- Battisti, D. S., E. S. Sarachik, and A. C. Hirst, 1999: A consistent model for the large-scale steady surface atmospheric circulation in the tropics. *J. Climate*, **12**, 2956-2964.
- Betts, A. K., 1983: Thermodynamics of mixed stratocumulus layers: Saturation point budgets. *J. Atmos. Sci.*, **40**, 2655-2670.
- Bond, N. A., 1992: Observations of planetary boundary-layer structure in the eastern equatorial Pacific. *J. Climate*, **5**, 699-706.
- Bretherton, C. S., P. Austin, and S. T. Siems, 1995: Cloudiness and marine boundary layer dynamics in the ASTEX Lagrangian experiments. Part II: Cloudiness, drizzle, surface fluxes, and entrainment. *J. Atmos. Sci.*, **52**, 2724-2735.
- Chelton, D. B., S. K. Esbensen, M. G. Schlax, N. Thum, M. H. Freilich, F. J. Wentz, C. L. Gentemann, M. J. McPhaden, and P. S. Schopf, 2001: Observations of coupling between surface wind stress and sea surface temperature in the eastern tropical Pacific. *J. Climate*, **14**, 1479-1498.
- Cronin, M. F., N. Bond, C. Fairall, J. Hare, M. J. McPhaden, R. A. Weller, 2002: Enhanced oceanic and atmospheric monitoring underway in eastern Pacific. *EOS, Transactions, AGU*, **83**(19), pages 205, 210-211.
- Deser, C., J. J. Bates and S. Wahl, 1993: The influence of sea surface temperature on stratiform cloudiness along the equatorial front in the Pacific Ocean. *J. Climate*, **6**, 1172-1180.
- Halpern, D., 1987: Observations of annual and El Niño thermal and flow variations at 0°, 110°W and 0°, 95°W during 1980-1985. *J. Geophys. Res.*, **92**, 8197-8212.
- Hashizume, H., S.-P. Xie, W. T. Liu and K. Takeuchi, 2001: Local and remote atmospheric response to tropical instability waves: A global view from space. *J. Geophys. Res.*, **106**, 10173-10185.
- Hashizume, H., S.-P. Xie, M. Fujiwara, M. Shiotani, T. Watanabe, Y. Tanimoto, W. T. Liu, and K. Takeuchi, 2002: Direct observations of atmospheric boundary layer response to SST variations associated with tropical instability waves over the eastern equatorial Pacific. *J. Climate*, **15**, 3379-3393.

- Hayes, S. P., M. J. McPhaden, and J. M. Wallace, 1989: The influence of sea surface temperature on surface wind in the eastern equatorial Pacific. *J. Climate*, **2**, 1500-1506.
- Kessler, W. S., G. C. Johnson, and D. W. Moore, 2002: Sverdrup and nonlinear dynamics of the Pacific Equatorial Currents. *J. Phys. Oceanogr.*, submitted.
- Lindzen, R. S., and S. Nigam, 1987: On the role of sea-surface temperature gradients in forcing low-level winds and convergence in the tropics. *J. Atmos. Sci.*, **44**, 2440-2458.
- Liu, W.T., X. Xie, P.S. Polito, S.-P. Xie, and H. Hashizume, 2000: Atmospheric manifestation of tropical instability waves observed by QuikSCAT and Tropical Rain Measuring Mission. *Geophys. Res. Lett.*, **27**, 2545-2548.
- Masina, S., S. G. H. Philander, and A. B. G. Bush, 1999: An analysis of tropical instability waves in a numerical model of the Pacific Ocean, 2, Generation and energetics of the waves. *J. Geophys. Res.*, **104**, 29637-29661.
- McPhaden, M. J., et al., 1998: The tropical ocean global atmosphere (TOGA) observing system: a decade of progress. *J. Geophys. Res.*, **103**, 14169-14240.
- Philander, S. G. H., 1978: Instabilities of zonal equatorial currents, 2. *J. Geophys. Res.*, **83**, 3679-3682.
- Qiao, L., and R. H. Weisberg, 1995: Tropical instability wave kinematics: observations from the tropical instability wave experiment. *J. Geophys. Res.*, **100**, 8677-8693.
- Raymond, D. J., C. Lopez-Carrillo, and L. L. Cavazos, 1998: Case-studies of developing east Pacific easterly waves. *Q. J. Roy. Meteorol. Soc.*, **124**, 2005-2034.
- Raymond, D. J., G. Raga, C. S. Bretherton, S. deSzoek, J. Molinari, C. Lopez-Carrillo, and Z. Fuchs, 2002: Dynamics of the intertropical convergence zone of the east Pacific. *J. Atmos. Sci.*, submitted.
- Small, R.J., S.-P. Xie and Y. Wang, 2003: Numerical simulation of atmospheric response to Pacific tropical instability waves. *J. Climate*, submitted.
- Thum, N., S. K. Esbensen, D. B. Chelton, and M. J. McPhaden, 2002: Air-sea heat exchange along the northern sea surface temperature front in the eastern tropical Pacific. *J. Climate*, **15**, 3361-3378.



- Wallace, J. M., T. P. Mitchell, and C. Deser, 1989: The influence of sea surface temperature on surface wind in the eastern equatorial Pacific: Seasonal and interannual variability. *J. Climate*, **2**, 1492-1499.
- Wentz, F. J., C. Gentemann, D. Smith, and D. Chelton, 2000: Satellite measurements of sea surface temperature through clouds. *Science*, **288**, 847-850.
- Xie, S.-P., M. Ishiwatari, H. Hashizume, and K. Takeuchi, 1998: Coupled ocean-atmospheric waves on the equatorial front. *Geophys. Res. Lett.*, **25**, 3863-3866.
- Yin, B., and B. A. Albrecht, 2000: Spatial variability of atmospheric boundary layer structure over the eastern equatorial Pacific. *J. Climate*, **13**, 1574-1592.

## Figure list

Fig. 1. Tropical sea surface temperature (SST) showing a well-developed tropical instability wave (TIW) on December 9, 2001. Data are from the Tropical Rain Measuring Mission (TRMM) satellite's microwave imager (TMI) and are averaged over 3 days.

Fig. 2. Regression of QuikSCAT winds and TMI SST to TIW bandpassed TMI SST at 2°N, 110°W for the 2001 TIW season (June 1-December 31), following the procedure of Hashizume et al. (2001). SST and wind anomalies are in units °C and  $\text{m s}^{-1} \text{ } ^\circ\text{C}^{-1}$ .

Fig. 3. Time series along 110°W of (a)  $P_0$  at 2°N (black) and 0° (grey), (b)  $T_s$  at 2°N (black) and 0° (grey), (c)  $\Delta P_0$ , and (d)  $\Delta T_s$  (black) and  $\Delta T_a$  (grey).  $\Delta$  denotes 2°N minus equatorial difference. Surface pressure ( $P_0$ ) has units hPa; air temperature ( $T_a$ ) and SST ( $T_s$ ) have units °C.

Fig. 4. Variance preserving spectra of (a)  $\Delta P_0$  (in units  $\text{hPa}^2$ ), (b)  $\Delta T_s$  (in units  $^\circ\text{C}^2$ ), (c)  $\Delta T_a$  (in units  $^\circ\text{C}^2$ ). Frequency is in units  $\text{days}^{-1}$ . Corresponding periodicities in unit days are shown for selected frequencies. 95% confidence limits are shown as thin lines.

Fig. 5. Coherence (top panels), transfer function in units ( $\text{hPa/K}$ ) (middle panels), and phase in units degrees (bottom panels) as a function of frequency for  $x = \Delta T_s$  and  $y = -\Delta P$  (left column) and  $x = \Delta T_a$  and  $y = -\Delta P$  (right column).

Fig 6. Advection of TIW meridional momentum in units  $10^{-6} \text{ m s}^{-2} \text{ } ^\circ\text{C}^{-1}$ , computed from June

through December 2001 mean winds and regressed winds shown in Fig. 2 (shaded). TIW regressed meridional winds in units  $\text{m s}^{-1} \text{ } ^\circ\text{C}^{-1}$  from Fig. 2 (contoured). Mean winds for June through December 2001 in units  $\text{m s}^{-1}$  (vectors).

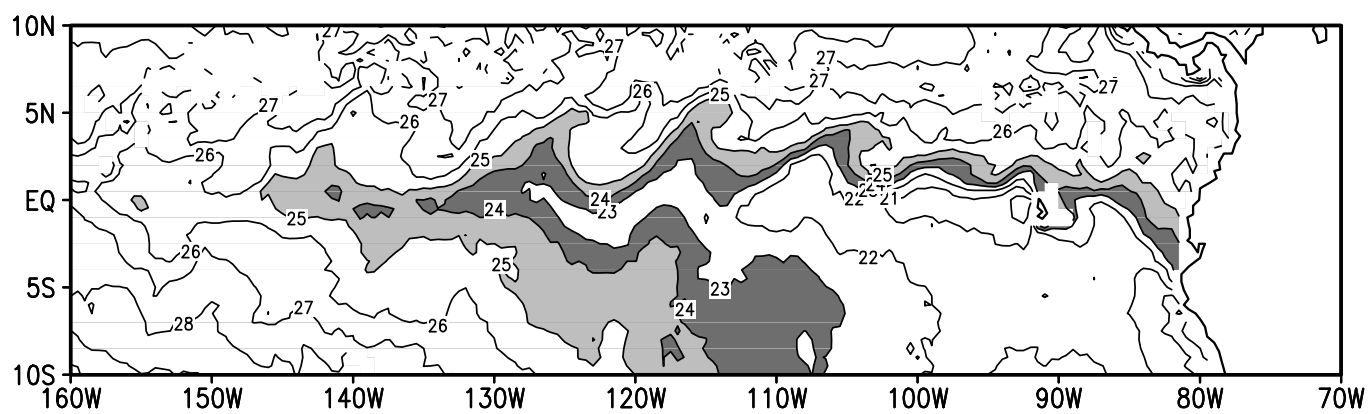


Figure 1

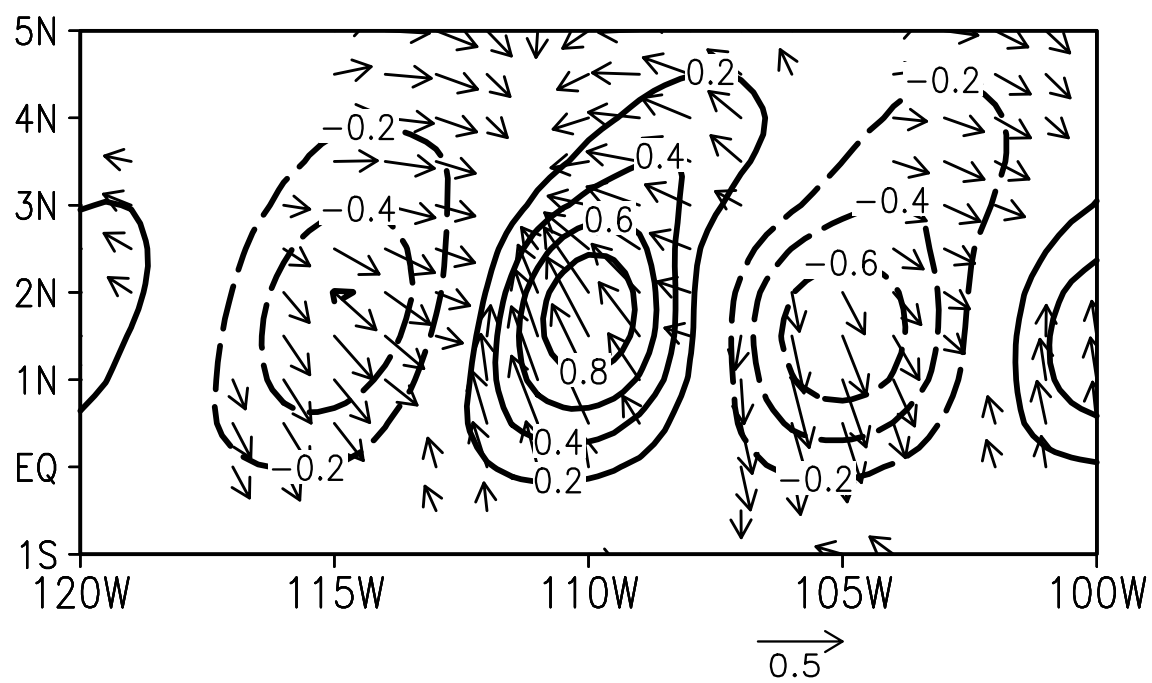


Figure 2

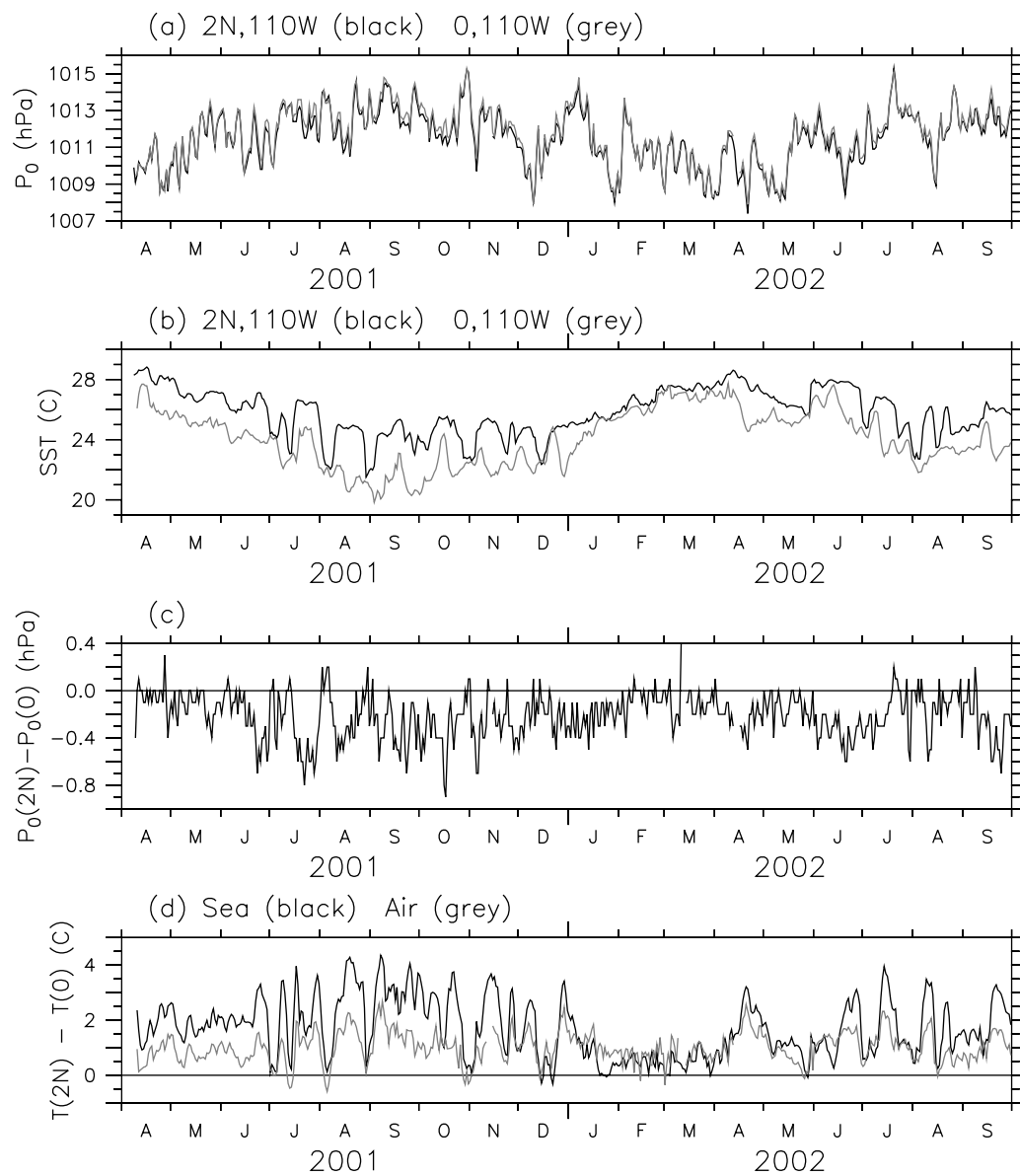


Figure 3

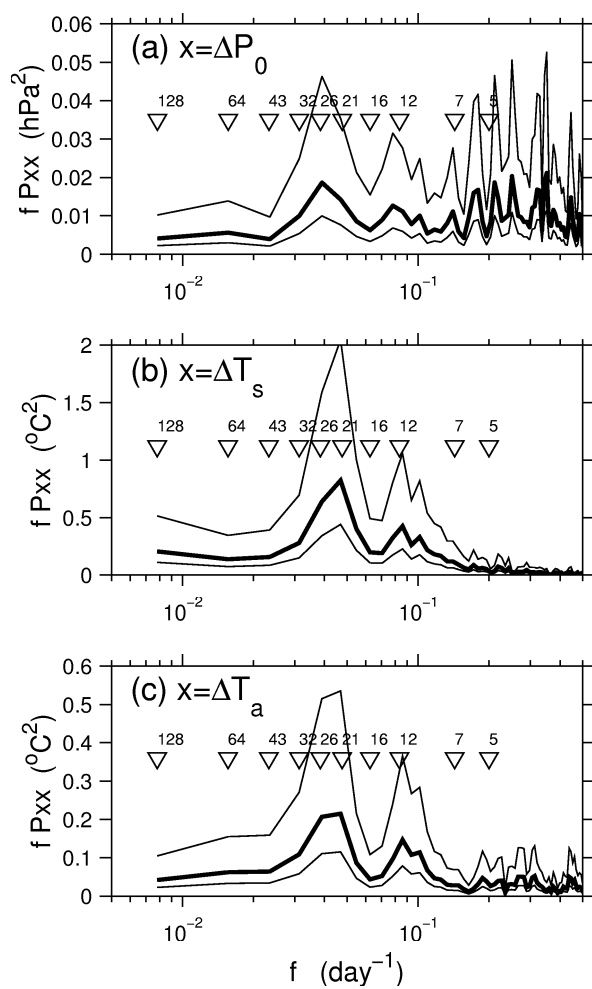


Figure 4

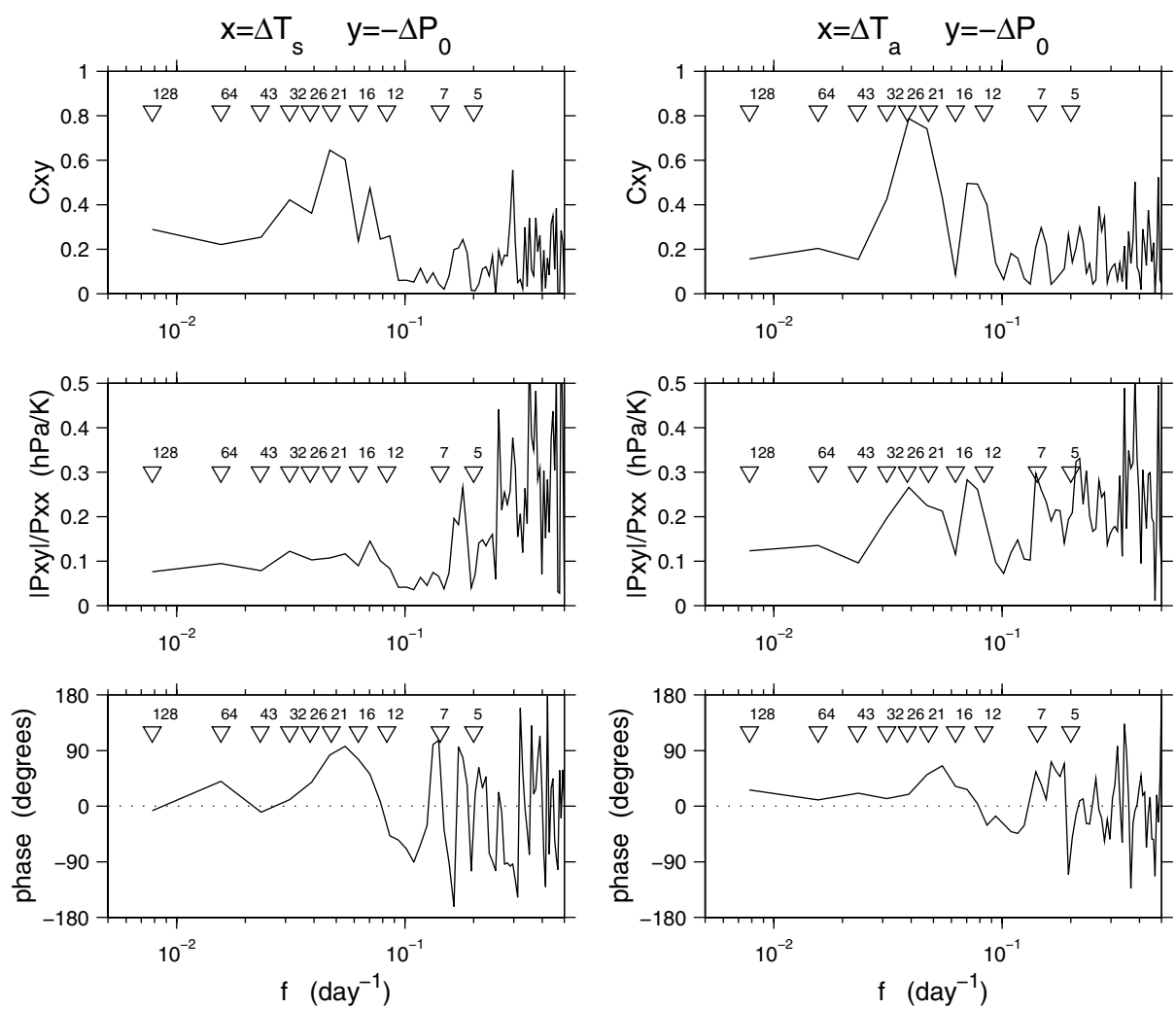


Figure 5



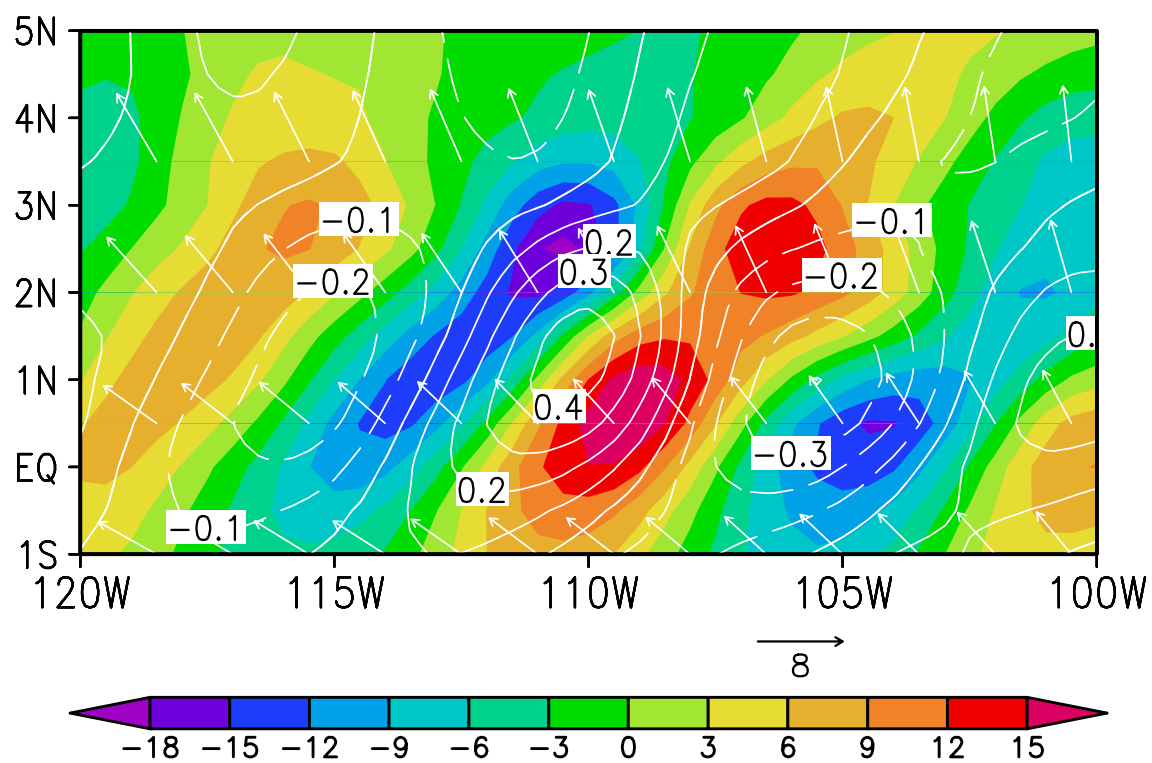


Figure 6